# Improving Simulation of Earth System Variability through Weakly Coupled Ocean Data Assimilation in E3SM

Pengfei Shi[1,*], L. Ruby Leung[1,*], Zhaoxia Pu[2], Samson Hagos[1], and Karthik Balaguru[1]

[1] *Atmospheric, Climate, and Earth Sciences Division, Pacific Northwest National Laboratory, Richland, Washington, USA*

[2] *Department of Atmospheric Sciences, University of Utah, Salt Lake City, Utah, USA*

[*] To whom correspondence may be addressed. Pengfei Shi (pengfei.shi@pnnl.gov) and L. Ruby Leung (Ruby.Leung@pnnl.gov)

**Abstract.** Accurate initialization of ocean states is essential for skillful prediction of Earth system variability across seasonal-to-decadal timescales. In this study, we evaluate the impact of a newly developed four-dimensional ensemble variational (4DEnVar)-based weakly coupled ocean data assimilation (WCODA) system within the DOE Energy Exascale Earth System Model version 2 (E3SMv2) on global and regional climate variability. By assimilating monthly ocean temperature and salinity from the EN4.2.1 reanalysis into the fully coupled model, we demonstrate substantial improvements in simulating both interannual and decadal climate variability. Compared with the free-running coupled simulation, the assimilation experiment exhibits markedly enhanced interannual correlations with observations for global mean surface air temperature and precipitation anomalies. The temporal variability of key climate modes, including ENSO, the Indian Ocean Dipole, and multidecadal variability in the Pacific and Atlantic Oceans, also shows markedly improved phase agreement with observations. Regional evaluation over the contiguous United States further shows enhanced skill in simulating winter surface air temperature and precipitation, particularly in the northern and southern regions, respectively, linked to improved ENSO simulation. Additional hindcast experiments initialized from the WCODA system exhibit no appreciable initialization shock in the early years and reproduce physically coherent ENSO teleconnection patterns, suggesting the dynamical consistency of the coupled initialization framework. These findings underscore the critical role of coupled forecasts in the data assimilation cycle for propagating observational information across Earth system components. By assimilating ocean reanalysis within the fully coupled framework, the WCODA system enables cross-component information exchange among the ocean, atmosphere, and land, thereby generating dynamically consistent initial conditions that support more accurate simulations of Earth system variability and lay the foundation for seasonal-to-decadal prediction applications.

**Deleted:** . These improvements contribute to more accurate simulations of Earth system variability across multiple timescales and lay the foundation for providing realistic initial conditions for seasonal-to-decadal prediction applications.

## 1. Introduction

Accurately representing climate variability across multiple timescales remains a major challenge in climate modeling and prediction. The initial conditions of the climate system, including the ocean, atmosphere, and land surface, play a crucial role in determining the accuracy and reliability of climate predictions (Boer et al., 2016; Taylor et al., 2012). Among these components, the ocean exhibits the longest memory and exerts a dominant influence on climate variability through its interactions with the atmosphere and other components (Wang, 2019). Therefore, improving the initialization of ocean states is widely recognized as a key approach for enhancing the skill of climate predictions (Meehl et al., 2021; Zhu et al., 2017).

Data assimilation methods have been developed to integrate observational data into coupled models, thereby generating realistic initial conditions and enhancing predictive skill. Traditionally, ocean data assimilation has been conducted in an uncoupled framework, where ocean observations are assimilated into a standalone ocean model forced by prescribed atmospheric forcing (Carton and Giese, 2008). The resulting ocean analyses are then combined with independently derived analyses from other uncoupled components (e.g., atmosphere and land) to construct the initial conditions for coupled models. However, because each component is initialized independently, this uncoupled approach often results in dynamical inconsistencies across multiple components, which can trigger initialization shock that degrades coupled model forecasts (Mulholland et al., 2015; Zhang, 2011). To address these limitations, recent studies have increasingly used coupled data assimilation (CDA) (Wu et al., 2018; Zhang et al., 2012).

CDA has emerged as an advanced framework for performing ocean data assimilation directly within the coupled model. CDA methods are generally categorized into weakly coupled data assimilation (WCDA) and strongly coupled data assimilation (SCDA). In WCDA, ocean observations or reanalysis products are assimilated separately into the ocean component during the analysis step, but the coupled model is utilized in the forecast step to transfer ocean observational information to other components through multi-component interactions (Browne et al., 2019). The fundamental distinction between WCDA and uncoupled data assimilation lies in whether a coupled model is employed in the forecast step to generate the background forecast. In WCDA, the background forecast is produced through the coupled model integration, while observations or reanalysis products are assimilated independently within each individual component. In contrast, uncoupled data assimilation utilizes standalone component models for both the forecast and analysis stages (Shi et al., 2024a; Zhang et al., 2020). Unlike uncoupled approaches, CDA produces more dynamically balanced and self-consistent initial conditions, thereby enhancing forecast skill (Feng et al., 2018; Shi et al., 2022). However, as a subcategory of CDA, WCDA neglects cross-component background error covariances during the analysis step, which limits its ability to explicitly correct coupled state errors (Tang et al., 2021). In contrast, SCDA leverages these covariances to facilitate cross-domain information propagation, allowing observational data in one component to instantaneously update the state variables of other components (Penny et al., 2019; Lin and Pu, 2020). By treating the coupled system as a unified entity, SCDA typically offers superior assimilation performance over WCDA (Han et al., 2013; Sluka et al., 2016; Lin and Pu, 2019). However, the practical implementation of SCDA faces considerable challenges, primarily owing to the difficulty of estimating cross-component background error covariances. Therefore, WCDA remains more widely adopted in current systems (Zhou et al., 2024).

The Energy Exascale Earth System Model (E3SM) is a state-of-the-art Earth system model developed by the U.S. Department of Energy to advance the understanding of Earth system variability and change (Leung et al., 2020). Recently, Shi et al. (2025) developed a new weakly coupled ocean data assimilation (WCODA) system utilizing the four-dimensional ensemble variational (4DEnVar) method. This 4DEnVar-based WCODA system is intended to provide realistic initial conditions for seasonal-to-decadal (S2D) hindcast experiments within the E3SM framework. The primary objective of this study is to evaluate the strengths and limitations of this newly developed WCODA system and to document its capability in capturing global and regional climate variability for the broader modeling community, with particular emphasis on large-scale climate modes and their remote impacts that are essential for S2D prediction applications. Specifically, this evaluation focuses on four key aspects: (1) surface air temperature and precipitation anomalies over ocean, land, and global domains; (2) major tropical variability, including the Indian Ocean Dipole (IOD) and El Niño-Southern Oscillation (ENSO); (3) decadal-to-multidecadal variability, such as the Pacific Decadal

Oscillation (PDO), Interdecadal Pacific Oscillation (IPO), and Atlantic Multidecadal Oscillation (AMO); and (4) regional climate variability over the contiguous United States.

The paper is structured as follows. Section 2 describes the E3SMv2 model, datasets, and experimental design. Section 3 presents the results from analyzing major modes of climate variability. Finally, the conclusions and discussion are provided in Section 4.

## 2. Model, data and experimental design

### 2.1 Model description

E3SMv2 is a fully coupled Earth system model that includes the atmospheric, ocean, sea ice, land and river transport components. The atmospheric component (EAMv2) is based on a spectral-element dynamical core with 72 vertical levels and is configured on a cubed-sphere grid with approximately 110 km horizontal resolution (Golaz et al., 2022). The ocean component (MPAS-O) employs an unstructured Voronoi mesh with horizontal spacing of ~60 km in the midlatitudes and ~30 km near the equator and poles, and includes 60 vertical layers using a z-star coordinate (Reckinger et al., 2015). The sea ice component (MPAS-SI) shares the same horizontal mesh with MPAS-O and provides detailed representations of sea ice thermodynamics and dynamics (Turner et al., 2022). The land component (ELMv2) simulates land surface energy and water fluxes, biophysical processes, and soil hydrological processes (Golaz et al., 2019). The river transport component (MOSARTv2) represents streamflow routing across river basins (Li et al., 2013). These five components are dynamically coupled through the CPL7 coupler, which facilitates the exchange of momentum, heat, and mass fluxes among model components (Craig et al., 2012). The detailed description and assessment of E3SMv2 can be found in Golaz et al. (2022).

### 2.2 Data assimilation scheme

The 4DEnVar method employed in the WCODA system is based on the dimension-reduced projection four-dimensional variational (DRP-4DVar) algorithm (Wang et al., 2010). In DRP-4DVar, the ensemble-based approach is used to replace the adjoint model traditionally required in standard 4DVar, thereby significantly reducing computational cost. The DRP-4DVar method determines the optimal state in the ensemble subspace by fitting observational data to model-generated ensemble samples within the four-dimensional assimilation window (Liu et al., 2011; Shi et al., 2021). Unlike nudging methods, which typically apply empirical relaxation terms to the model's prognostic equations, the DRP-4DVar scheme obtains the optimal analysis by minimizing the cost function of 4DVar. Specifically, observational information is assimilated along the trajectory of the model solution within the four-dimensional assimilation window, ensuring that the optimal analysis is dynamically consistent with the model physics (He et al., 2017). To mitigate ensemble collapse, the DRP-4DVar algorithm employs an inflation technique that introduces a zero initial condition perturbation sample to reconstruct the ensemble projection space as a full-rank matrix (Wang et al., 2010). Due to its flexibility and efficiency, the DRP-4DVar method has been widely applied in diverse numerical models to improve the initialization of ocean, land, and atmospheric states (He et al., 2020; Shi et al., 2024b; Zhu et al., 2022). In particular, the DRP-4DVar approach has been shown to generate dynamically consistent initial conditions that effectively mitigate the initialization shock during the early years of initialized hindcasts (He et al., 2017).

In this study, monthly mean ocean temperature and salinity from the EN4.2.1 reanalysis (Good et al., 2013) are assimilated into the ocean component of the fully coupled E3SMv2 model within a one-month assimilation window. The observational uncertainty of the EN4.2.1 reanalysis is represented through the observation error covariance matrix, which is statistically derived from the variance of ocean temperature and salinity data. The spatiotemporal density of observations within the EN4.2.1 product modulates the assimilation impact. Regions with dense observational coverage are expected to exhibit more pronounced improvements, whereas in data-sparse areas such as the Indian Ocean, the assimilation constraint is relatively weaker. Each monthly assimilation cycle consists of the analysis and forecast stages. First, the fully coupled E3SMv2 model is run forward for one month using the background initial conditions to generate model-derived monthly means of ocean temperature and salinity. In the analysis stage, the differences between these model outputs and the EN4.2.1 reanalysis are calculated to form the observational innovation. The DRP-4DVar scheme then applies this innovation to compute the optimal initial conditions for the ocean component at the beginning of the assimilation cycle. During the following forecast stage, the fully coupled model is rewound to the start of the month and re-integrated for the same month using the optimized ocean state and the background fields from other components. Through this coupled forecast, ocean observational information is dynamically propagated to influence the state variables of other components (e.g., atmosphere and land) through multi-component interactions. Thus, while the assimilation is confined to the ocean, employing the fully coupled E3SMv2 model in the forecast stage enables the transfer of assimilated ocean information to other Earth system components, classifying this system as a WCDA framework (Zhang et al., 2020). Further technical details of the assimilation system are described in Shi et al. (2025).

### 2.3 Numerical experiments

Two numerical experiments are conducted to assess the impact of the WCODA system on climate variability: a control experiment (CTRL) and an assimilation experiment (ASSIM). Both experiments are initialized from the same initial condition on January 1, 1950, which is derived from a fully spun-up long-term integration of E3SMv2 (Golaz et al., 2022). Following initialization, the CTRL experiment is integrated freely without re-initialization or further modifications to the model state from 1950 to 2021 under observed historical external forcings. This experiment serves as the reference simulation for evaluating the influence of the assimilation system. Both CTRL and ASSIM experiments are forced with the same historical external forcings prescribed by the CMIP6 protocol (Eyring et al., 2016). The E3SMv2 model had already reached a stable quasi-equilibrium state through a long spin-up and historical integration (Golaz et al., 2022).

The ASSIM experiment assimilates monthly mean ocean temperature and salinity from the EN4.2.1 reanalysis into all 60 layers of the ocean component in the fully coupled E3SMv2 model from 1950 to 2021 using a one-month assimilation window. At the beginning of each month, monthly mean ocean temperature and salinity from the EN4.2.1 reanalysis are assimilated to update the ocean initial conditions, after which the fully coupled model is integrated freely until the end of the month. During this forecast period, the assimilated ocean information is dynamically propagated to other components through multi-component interactions. Unlike the sea surface temperature (SST) relaxation approach used in pacemaker experiments to isolate the ocean influence on climate variability (e.g., Kosaka and Xie, 2016), the assimilation system is implemented to generate initial conditions for hindcast experiments by incorporating full-depth ocean temperature and salinity reanalysis to constrain the complete three-dimensional ocean state. This approach preserves vertical dynamical consistency and retains the subsurface ocean memory necessary for capturing decadal-to-multidecadal variability. For example, Morioka et al. (2018) demonstrated that skillful prediction of decadal variability in the South Atlantic requires the assimilation of subsurface ocean temperature and salinity, as SST-only assimilation fails to accurately represent zonal heat transport. However, the Arctic Ocean is excluded from the assimilation domain due to sparse observational coverage and the current absence of a coupled ice-ocean assimilation scheme. Much of the Arctic Ocean is characterized by pervasive year-round sea ice cover. Without simultaneously updating sea ice variables, assimilating ocean temperature and salinity alone could potentially introduce physical inconsistencies at the ice-ocean interface. Addressing this technical limitation remains a high priority for future system development.

### 2.4 Evaluation datasets

Three types of monthly reanalysis datasets are used for evaluation: 1) ERA5 reanalysis data, including surface air temperature, 850 hPa winds, and 500 hPa geopotential height. ERA5 incorporates a wide range of satellite and in situ observations to produce high-quality global atmospheric fields (Hersbach et al., 2020). 2) Global Precipitation Climatology Project (GPCP) monthly precipitation data. This dataset provides reliable global precipitation estimates based on satellite microwave, infrared measurements, and surface rain gauge data (Adler et al., 2003). 3) Hadley Centre Sea Ice and Sea Surface Temperature (HadISST) data. HadISST provides monthly SST analyses derived from a combination of in situ measurements and satellite-based retrievals (Rayner et al., 2003). Since the HadISST dataset and the assimilated EN4.2.1 reanalysis partially share a common pool of underlying in situ ocean observations, HadISST does not serve as a fully independent validation dataset. Nevertheless, the improved agreement with HadISST still demonstrates the effectiveness of the assimilation system in constraining the ocean states.

## 3. Results

### 3.1 Surface air temperature and precipitation

The temporal evolution of both non-detrended and linearly detrended annual mean surface air temperature anomalies over the ocean, land, and global domains is shown in Fig. 1. The non-detrended time series (Figs. 1a-c) suggest the long-term warming trend, while the detrended series (Figs. 1d-f) isolate interannual variability by removing the linear trend from each domain-averaged time series. In both cases, ASSIM better captures the observed interannual surface air temperature variability compared to CTRL across all domains. For the non-detrended global annual mean surface air temperature, the correlation of ASSIM with observations is 0.92, slightly higher than the value of 0.85 reported by Douville et al. (2015) in their tropical Pacific pacemaker experiment. After linear detrending, the correlation coefficient between ASSIM and observations reaches 0.47 over the ocean, much higher than that of CTRL (0.09). Over land and global domains, the correlation coefficients for ASSIM are 0.44 and 0.49, respectively, again exceeding those of CTRL (land/global: 0.26/0.18). All three detrended correlations from ASSIM pass the 95% confidence level, indicating statistically significant improvements in simulating interannual surface temperature variability. The improvement is most pronounced over the ocean, where the assimilated ocean state exerts a direct influence on near-surface atmospheric conditions. Notably, the improved correlations over land suggest that the benefits of ocean data assimilation extend beyond oceanic regions, reflecting its broader influence on global surface temperature variability. However, compared with pacemaker experiments in which SST is directly nudged within the tropical Pacific, the relatively weaker atmospheric response to certain ENSO events in ASSIM may be related to the competing influence of global ocean constraints beyond the tropical Pacific, as well as the smoothing effect introduced by the monthly assimilation window.

Figure 2 displays the spatial distribution of climatological mean differences in surface air temperature. Compared to observations, CTRL exhibits widespread cold biases over the tropical and subtropical oceans, as well as notable warm biases at high latitudes. In contrast, these biases are significantly reduced in ASSIM, particularly over the North Pacific, North Atlantic, and the midlatitude Southern Ocean. Specifically, the cold bias in the North Pacific decreases from -1.81 °C in CTRL to -0.76 °C in ASSIM, and from -3.23 °C to -1.09 °C in the North Atlantic. The warm bias over the midlatitude Southern Ocean is notably reduced from 1.07 °C in CTRL to 0.13 °C in ASSIM. Improvements are also evident over land regions, such as eastern China, northern Eurasia, northern Africa, and parts of North America. The spatial pattern of reduced surface air temperature bias closely aligns with the reduction in SST bias reported by Shi et al. (2025), highlighting the strong coupling between the ocean surface and the atmosphere. However, the current assimilation experiment does not explicitly isolate the respective contributions of SST and subsurface ocean states. Future SST-only assimilation experiments would be needed to disentangle their individual effects on surface air temperature. The climatological warm biases over the Arctic Ocean appear slightly enhanced in ASSIM compared with CTRL. Since the Arctic Ocean state is not directly constrained by assimilation, it may respond indirectly to remote adjustments introduced elsewhere, potentially leading to a redistribution of temperature biases. Despite this localized degradation, the assimilation maintains the overall stability of the coupled system. As shown in Fig. A1, key global mean diagnostics, including top-of-atmosphere net energy flux, surface air temperature, ocean temperature and salinity, remain stable throughout the ASSIM integration.

The interannual variability of linearly detrended precipitation anomalies over the ocean, land, and global domains is illustrated in Fig. 3. Compared with CTRL, ASSIM shows markedly improved agreement with the observed interannual precipitation variability across all three domains. Specifically, the temporal correlations with observations increase from 0.11 in CTRL to 0.52 in ASSIM over the ocean and from 0.27 in CTRL to 0.60 in ASSIM over land. At the global scale, the correlation rises from 0.04 in CTRL to 0.55 in ASSIM. All three correlations from ASSIM are statistically significant at the 95% confidence level. These results suggest that assimilating observed ocean states enhances the simulation of interannual precipitation variability over both ocean and land, with the latter improvement possibly related to atmospheric circulation and moisture transport.

Figure 4 shows the spatial distribution of climatological mean precipitation and associated model biases. In the observation (Fig. 4a), major precipitation maxima are located along the Intertropical Convergence Zone (ITCZ) in the equatorial Pacific, the South Pacific Convergence Zone (SPCZ) extending southeastward from the western Pacific, and the tropical Indian Ocean. A dry zone is also evident along the west coast of South America. Compared with observations, CTRL overestimates precipitation over the central Pacific and the southern equatorial Atlantic, and significantly underestimates rainfall over the tropical eastern Indian Ocean and the northern equatorial Atlantic (Figs. 4b & d). In contrast, these biases are substantially reduced in ASSIM (Figs. 4c & e). Precipitation in the tropical eastern Indian Ocean is enhanced, resulting in better agreement with observations. Moreover, in the tropical Atlantic, the dry bias over the northern equatorial Atlantic is reduced from -1.27 mm/day in CTRL to -0.34 mm/day in ASSIM, while the wet bias over the southern equatorial Atlantic decreases from 1.81 mm/day to 0.62 mm/day. These reductions in systematic biases bring the climatological precipitation in ASSIM into better agreement with observations. Over some regions, particularly the tropical Pacific, the residual differences are no longer statistically significant. The improvement in tropical precipitation is closely linked to changes in the large-scale meridional circulation. As illustrated in Fig. A2, CTRL exhibits an anomalously strong ascending branch of the Hadley circulation in the northern tropics, which sustains a pronounced wet bias over the tropical Pacific. In contrast, this anomalous ascent is effectively suppressed in ASSIM, contributing to a more realistic precipitation distribution across the tropical and subtropical regions.

### 3.2 ENSO

ENSO is the dominant mode of interannual climate variability in the tropics and exerts profound impacts on global atmospheric circulation (Chiang and Sobel, 2002). ENSO variability is commonly monitored by the Niño 3.4 index, defined as the SST anomalies averaged over the equatorial central Pacific (5°S–5°N, 170°W–120°W) (Trenberth and Stepaniak, 2001). To evaluate the representation of ENSO variability, we analyze the temporal evolution of the monthly and winter Niño 3.4 index (Fig. 5). As expected, CTRL exhibits very weak correlations with observations, with correlation coefficients of only 0.02 for the monthly and 0.07 for the winter Niño 3.4 index, indicating poor phase agreement with the observed Niño 3.4 index. Compared with CTRL, ASSIM exhibits markedly improved phase agreement with the observed ENSO variability. The temporal evolution of the Niño 3.4 index in ASSIM closely matches the observation, with correlations increasing to 0.87 for the monthly and 0.95 for the winter index. These results demonstrate that ocean data assimilation provides an effective constraint on tropical Pacific SST variability.

Figure 6 further evaluates ENSO characteristics through the power spectra and seasonal cycle of the monthly Niño 3.4 index. The observed spectrum exhibits a pronounced peak in the 3–5 year band, consistent with typical ENSO periodicities (Fig. 6a). This spectral feature is reasonably well reproduced in ASSIM (Fig. 6b). By comparison, CTRL underestimates the variance in this band and produces an unrealistically amplified peak at 2–3 years (Fig. 6c). Beyond its frequency characteristics, ENSO also exhibits a strong seasonal cycle. The observed Niño 3.4 index shows minimum variance in April and peak amplitude in December, reflecting the well-known phase-locking behavior of ENSO (Fig. 6d). ASSIM captures this seasonal cycle well, although the minimum occurs one month later (Fig. 6e). In contrast, CTRL exhibits a flatter seasonal cycle with markedly weaker variance during the winter peak, and its seasonal minimum is delayed by two months (Fig. 6f).

To further assess the representation of ENSO-related atmospheric variability, we examine the Southern Oscillation Index (SOI), which reflects the east–west seesaw pattern in sea level pressure (SLP) between the western and eastern tropical Pacific. The SOI is commonly defined as the normalized difference in SLP anomalies between Tahiti and Darwin, and serves as the atmospheric counterpart to the Niño 3.4 index (Hanley et al., 2003). Figure 7 presents the temporal evolution of the monthly and winter SOI from the observation, ASSIM, and CTRL. The observed SOI exhibits pronounced interannual fluctuations associated with ENSO phases. Consistent with its poor simulation of the Niño 3.4 index, CTRL fails to capture the observed SOI variability, with correlations of -0.02 for the monthly and -0.04 for the winter index. In contrast, ASSIM reproduces the SOI variability more realistically, with correlations increasing to 0.40 for the monthly and 0.62 for the winter index. These results indicate that assimilating ocean reanalysis not only constrains SST but also enhances the phase agreement of ENSO-related atmospheric variability with observations in coupled models.

### 3.3 IOD

The Indian Ocean Dipole (IOD) is a prominent mode of interannual variability in the tropical Indian Ocean that strongly influences surrounding climate systems (Saji et al., 2006). It typically begins to develop in boreal summer and reaches its peak during autumn. A widely used metric for quantifying IOD variability is the Dipole Mode Index (DMI), defined as the difference in SST anomalies between the western (50°E–70°E, 10°S–10°N) and eastern (90°E–110°E, 0°–10°S) equatorial Indian Ocean (Saji et al., 1999). The temporal evolution of the autumn DMI is further shown in Fig. 8. The observed DMI exhibits pronounced interannual variations associated with alternating positive and negative IOD phases. The CTRL simulation substantially overestimates the IOD amplitude and shows a weak correlation of -0.11 with observations. Such overestimation is the common bias in coupled climate models, as noted in previous studies (Ju et al., 2025). In contrast, ASSIM shows notable improvements in both the amplitude and temporal variability of the DMI, with the correlation increasing to 0.56 and passing the 95% confidence level. These results highlight the effectiveness of ocean data assimilation in improving the temporal agreement of IOD variability with observations. Nevertheless, the lower DMI correlation in ASSIM compared with that of the Niño 3.4 index is partly attributable to known limitations of the assimilated EN4.2.1 dataset in the Indian Ocean. As noted by Good et al. (2013), the EN4.2.1 reanalysis exhibits regional deficiencies in this basin due to the limited availability of near-surface observations that meet quality-control standards, thereby limiting the assimilation effectiveness in the Indian Ocean.

### 3.4 PDO, IPO, AMO

The Pacific Decadal Oscillation (PDO) is the leading mode of decadal SST variability in the North Pacific, characterized by basin-scale SST anomalies that typically persist for one to two decades. The PDO index is derived as the leading empirical orthogonal function (EOF) mode of detrended SST anomalies over the North Pacific (20°–70°N, 110°E–100°W) (Mantua et al., 1997). The EOF analysis is performed separately for the observations and each model experiment. Prior to the EOF calculation, all observational datasets and model outputs are interpolated onto a common horizontal grid and linear trends are removed at each grid point. Figure 9 illustrates both the temporal evolution and spatial pattern of the annual PDO index from 1965 to 2016. The observed PDO index displays a canonical sequence of phase transitions: a cool phase before the late 1970s, a persistent warm phase extending into the late 1990s, and a return to negative values thereafter (Fig. 9a). These decadal transitions are reasonably captured by ASSIM, yielding a temporal correlation of 0.67 with observations (Fig. 9b). In contrast, CTRL fails to reproduce the observed phase transitions, with a much lower correlation of 0.19 (Fig. 9c). Besides the temporal evolution, the spatial structure of the PDO index is also analyzed. The observed pattern exhibits a horseshoe-shaped structure with cold anomalies in the central North Pacific and warm anomalies along the western coast of North America (Fig. 9d). This spatial pattern is well reproduced in ASSIM, with a spatial correlation of 0.90 (Fig. 9e). However, the PDO pattern from CTRL exhibits a distorted structure, and its spatial correlation decreases to 0.68 (Fig. 9f). These improvements in both the temporal evolution and spatial structure of the PDO underscore the potential of the assimilation system to enable more skillful decadal climate predictions by providing improved initial states.

Beyond the North Pacific, another major mode of decadal variability affecting the entire Pacific basin is the Interdecadal Pacific Oscillation (IPO). Similar to the PDO, the IPO index is obtained from the leading EOF mode of detrended SST anomalies, but computed over the whole Pacific (50°S–50°N, 100°E–70°W) (Doblas-Reyes et al., 2013). The annual evolution of the IPO index is shown in Fig. 10, indicating the basin-wide coherence of Pacific decadal variability. The observed IPO index undergoes distinct decadal shifts, including a negative phase prior to the late 1970s, a prolonged positive phase extending through the 1980s and 1990s, and a return to negative values in the early 2000s. These phase transitions are closely reproduced by ASSIM, which achieves a high temporal correlation of 0.80 with observations. On the other hand, CTRL fails to track the decadal evolution of the observed IPO and shows a much weaker correlation of 0.20. These results indicate that ocean data assimilation serves as an effective pathway for constraining Pacific-basin SST variability and enhancing the phase alignment of the observed Pacific SST variability on decadal timescales.

In addition to the Pacific, the North Atlantic also exhibits notable low-frequency SST variability characterized by the Atlantic Multidecadal Oscillation (AMO). The AMO index is computed as the linearly detrended SST anomalies averaged over the North Atlantic (0–60°N, 0–80°W) (Trenberth and Shea, 2006). Figure 11 presents the temporal evolution of the annual AMO index from 1965 to 2016. The observed AMO index shows a pronounced negative phase in the 1970s and 1980s, followed by a persistent positive phase beginning in the mid-1990s. These phase transitions are more accurately reproduced in ASSIM than in CTRL, particularly the timing and amplitude of the warm shift after the mid-1990s. The temporal correlation with observations is 0.71 in ASSIM, much higher than 0.17 in CTRL. This improved phase agreement of AMO variability in ASSIM reinforces its potential for better predicting related climate impacts over the North Atlantic and adjacent regions.

**3.5 U.S. T2m and Precipitation**

Building on the improved representation of tropical SST variability through ocean data assimilation, we extend our analysis to assess its impact on regional climate over land via teleconnections. Given the well-established influence of ENSO on U.S. winter climate variability (Ropelewski and Halpert, 1986; Higgins et al., 2000), we evaluate model performance in simulating interannual temperature and precipitation variability over the contiguous U.S. during boreal winter (Figs. 12 & 13). For winter surface air temperature (Fig. 12), ASSIM exhibits widespread increases in temporal correlation with observations across large portions of the northern and western U.S., particularly over the Intermountain West and Great Lakes regions. In these areas, correlation improvements commonly exceed 0.3 and locally surpass 0.4. Consistent with the correlation patterns, RMSE reductions in ASSIM are also evident across the northern and central U.S., with maximum decreases up to 0.6 °C over the central Great Plains.

In contrast to temperature, improvements in winter precipitation simulations are more localized but remain pronounced across the southern U.S. (Fig. 13). Compared with CTRL, ASSIM shows higher correlations with observed precipitation over the Southwest, southern Great Plains, and Southeast. In particular, significant enhancements are evident in parts of

California, Texas, and Alabama, where correlation increases exceed 0.4 and locally approach 0.5. These correlation improvements are accompanied by consistent reductions in RMSE across similar regions. Notably, the largest RMSE reductions, exceeding 0.45 mm/day, are found over coastal California. The spatial coherence of these improvements suggests that incorporating realistic ocean states can better capture U.S. winter precipitation variability.

To further investigate the mechanisms underlying the improved simulation of U.S. winter climate, we examine the regression of surface air temperature and precipitation onto the Niño 3.4 index during boreal winter (Fig. 14). Boreal winter is the focus of this analysis because ENSO teleconnections to North America are strongest and most coherent during winter, while ENSO-related impacts in other seasons are generally weaker and less spatially coherent over the U.S. (Ropelewski and Halpert, 1986; Higgins et al., 2000). The Niño 3.4 index is calculated separately from its corresponding dataset, and all regressions are performed using simultaneous winter averages. The observed patterns reveal that ENSO exerts a pronounced influence on U.S. winter climate through large-scale atmospheric responses. During El Niño events, positive geopotential height anomalies dominate the northern part of the continent, which may suppress the southward intrusion of cold air masses. This circulation pattern could lead to anomalous warming across the northern U.S., producing significant positive correlations with ENSO in these regions (Fig. 14a). Meanwhile, strengthened subtropical westerlies enhance moisture transport into the southern U.S., favoring increased precipitation and yielding strong positive correlations with ENSO across the southern tier of the country (Fig. 14d).

These ENSO-related spatial structures are well reproduced in ASSIM (Figs. 14b & e). In particular, the regression patterns of temperature and precipitation in ASSIM closely resemble those in the observations, especially across the northern and southern U.S., respectively. The spatial pattern correlation between ASSIM and observations is 0.86 for surface air temperature, much higher than that of CTRL (0.35). For precipitation, the spatial correlation increases from 0.67 in CTRL to 0.72 in ASSIM. Furthermore, the regions with robust ENSO-related signals in ASSIM largely overlap with areas showing improved correlation and reduced RMSE in Figs. 12 and 13. The stippled regions in these figures denote statistically significant differences at the 95% confidence level. Specifically, for winter surface air temperature, statistically significant increases in correlation and concurrent reductions in RMSE are primarily found in parts of Arizona and Iowa (Fig. 12), while for winter precipitation, such improvements are mainly located over parts of California and Alabama (Fig. 13). To account for the potential delayed impact of ENSO, a one-month lagged regression analysis is also presented in Fig. A3. The resulting lagged patterns are highly consistent with the simultaneous winter regression results (Fig. 14), reinforcing the linkage between ENSO variability and U.S. winter climate anomalies. These results demonstrate that the improved phase alignment of ENSO variability enhances the simulation of U.S. winter surface air temperature and precipitation.

## 4 Conclusions

Accurate representation of climate variability across multiple timescales is essential for enhancing the reliability of Earth system predictions. One key factor influencing climate variability is the ocean state due to its long memory and strong coupling with the atmosphere. While ocean data assimilation has proven effective in improving ocean state estimates, many existing systems remain uncoupled and thus have limited ability to support coupled forecasts due to imbalances across multiple components (Mulholland et al., 2015; Zhang, 2011). To address this limitation, a new 4DEnVar-based WCODA system has been implemented within the E3SM model to provide dynamically consistent initial conditions for S2D hindcast experiments. Despite this progress, the specific impact of this WCODA system on the simulation of multiscale climate variability requires further evaluation. This study aims to thoroughly document the capabilities and limitations of this WCODA system in simulating global and regional climate variability, and to demonstrate its potential for improving initialization quality and predictive skill in coupled Earth system models.

Our results show that the WCODA system significantly improves the phase agreement of both interannual and decadal climate variability with observations. Beyond phase alignment, minor but noteworthy improvements are also found in representing the modes of variability, as indicated by the improved Niño3.4 spectrum, PDO EOF pattern, and ENSO teleconnection response over the contiguous U.S. Significant enhancements are achieved in capturing interannual variability and reducing model biases of surface air temperature and precipitation over land and ocean domains. Notably, the temporal evolution of major climate modes, including ENSO, IOD, PDO, IPO, and AMO, is markedly improved. In addition to better capturing the temporal evolution of various modes, the assimilation experiment also improves the power spectra and seasonal cycle of ENSO and the spatial pattern of PDO. Furthermore, regional evaluations over the contiguous U.S. reveal increased skill in reproducing the observed interannual variability of winter surface air temperature in the northern U.S. and precipitation in the southern regions, respectively. The improved simulation of U.S. winter temperature and precipitation is closely associated with better-simulated ENSO variability, as supported by the spatially coherent regression patterns of U.S. winter surface air temperature and precipitation onto the Niño 3.4 index. These findings demonstrate the capability of the WCODA system to deliver more skillful simulations of Earth system variability through improved ocean initial states and cross-component information exchange. It should be noted that these improvements primarily reflect enhanced phase alignment of internal variability with observations, and the monthly assimilation increments may introduce localized effects.

Despite these promising results, several limitations remain and offer opportunities for future development. The current assimilation system does not incorporate atmospheric or sea ice observations, which may limit its ability to fully constrain the coupled model states. While our results demonstrate that assimilating ocean reanalysis provides a sufficient constraint to improve the phase alignment of key climate modes, incorporating additional observational constraints from the atmosphere and sea ice may further enhance the representation of coupled climate variability and associated regional impacts. It should be noted that the improved temporal correlations primarily reflect enhanced phase alignment of the model's internal variability with observations, rather than intrinsic changes in modes of variability. Furthermore, as a weakly coupled system, the current WCODA framework does not explicitly account for cross-component background error covariances during the analysis step. Transitioning toward a SCDA framework would further improve the physical consistency and accuracy of the generated initial conditions.

Looking ahead, the WCODA system provides a promising foundation for improving the initialization of large-ensemble S2D hindcast experiments. To assess the quality of the resulting initial conditions, additional hindcast experiments were conducted at five-year intervals from 1981 to 2006 (Figs. A4 & A5). As shown in Fig. A4, the ensemble mean hindcasts initialized from the WCODA system closely track the observed annual mean global average surface air temperature anomalies, with no appreciable initialization shock during the early years of the hindcasts. The dynamical consistency of the WCODA-generated initial conditions is further supported by the well-reproduced ENSO teleconnection patterns in both the assimilation experiment (Fig. 14) and the initialized hindcasts (Fig. A5). Specifically, the regression patterns of winter surface air temperature and precipitation onto the Niño 3.4 index in the hindcasts (Fig. A5) closely resemble the observed and ASSIM patterns. These results suggest that the 4DEnVar-based WCODA system is capable of producing dynamically consistent initial conditions in which ocean information is transferred to other Earth system components through multi-component interactions, and the hindcasts initialized from these dynamically balanced initial conditions preserve similar teleconnection patterns as in the assimilation run.

The capacity of this 4DEnVar-based WCODA system to mitigate initialization shock and maintain cross-component dynamical consistency is particularly noteworthy when contrasted with traditional ocean-only initialized decadal prediction systems. A well-recognized limitation of ocean-only initialization is that ocean initial conditions are generated independently of the atmosphere and land, resulting in dynamical imbalances across components that can trigger pronounced initialization shock and rapid drift in the early years of the hindcasts (Chikamoto et al., 2019; Meehl et al., 2021; Kim et al., 2025). In contrast, by performing data assimilation within the fully coupled E3SMv2 framework, ocean observational information is propagated to other components through multi-component interactions during the coupled forecast step. Furthermore, the DRP-4DVar increments are derived by fitting the oceanic analysis within the four-dimensional assimilation window along the trajectory of the fully coupled model rather than the standalone ocean model. These features promote more dynamically consistent initial conditions across model components, thereby offering a practical pathway for reducing the initialization shock. Given that the assimilation of subsurface ocean temperature and salinity is essential for skillful decadal prediction (Morioka et al., 2018; Chikamoto et al., 2019), future efforts could explore systematic comparisons with SST-based pacemaker experiments to elucidate the distinct roles of surface and subsurface ocean constraints. Such comparisons would provide valuable insights into the mechanisms governing decadal predictability and inform the design of more effective initialization strategies. Ultimately, these advances will contribute to the development of more reliable seamless climate prediction systems with broad implications for climate services and society.

*Code and data availability.* The E3SMv2 source code is freely available under an open-source license and can be accessed via Zenodo at https://zenodo.org/records/16652680. The ERA5 reanalysis datasets are accessible from the Copernicus Climate Change Service through the Climate Data Store portal: https://cds.climate.copernicus.eu/datasets/reanalysis-era5-single-levels-monthly-means?tab=download (Hersbach et al., 2020). Monthly GPCP precipitation data can be obtained from https://psl.noaa.gov/data/gridded/data.gpcp.html (Adler et al., 2003). HadISST sea surface temperature data are available at https://www.metoffice.gov.uk/hadobs/hadisst (Rayner et al., 2003) and EN4.2.1 ocean temperature and salinity data can be accessed from https://www.metoffice.gov.uk/hadobs/en4 (Good et al., 2013). Model outputs are available on Zenodo at https://zenodo.org/records/16740831.

*Author contributions.* PS and LRL designed the experiments. PS developed the ocean data assimilation system and performed the model simulations. PS and LRL analyzed the results. PS and LRL drafted the initial manuscript. ZP, SH, and KB contributed to manuscript revisions.

*Competing interests.* The authors declare no competing interests.

*Acknowledgements*. This research was supported by the Office of Science, U.S. Department of Energy Biological and Environmental Research (BER) as part of the Water Cycle: Modeling of Circulation, Convection, and Earth System Mechanisms (WACCEM) Scientific Focus Area funded by the Regional and Global Model Analysis program area. Pacific Northwest National Laboratory is operated by Battelle Memorial Institute for the U.S. Department of Energy under contract DE-AC05-76RL01830. This research used computing resources of the National Energy Research Scientific Computing Center, which is supported by the Office of Science of the U.S. Department of Energy under Contract No. DE-AC02-05CH11231, and the BER Earth and Environmental System Modeling program's Compy computing cluster located at Pacific Northwest National Laboratory.

## REFERENCES


Adler, R. F., Huffman, G. J., Chang, A., Ferraro, R., Xie, P. P., Janowiak, J., Rudolf, B., Schneider, U., Curtis, S., Bolvin, D., Gruber, A., Susskind, J., Arkin, P., and Nelkin, E.: The version-2 Global Precipitation Climatology Project (GPCP) monthly precipitation analysis (1979–present), Journal of Hydrometeorology, 4, 1147–1167, https://doi.org/10.1175/1525-7541(2003)004<1147:TVGPCP>2.0.CO;2, 2003.

Boer, G. J., Smith, D. M., Cassou, C., Doblas-Reyes, F., Danabasoglu, G., Kirtman, B., Kushnir, Y., Kimoto, M., Meehl, G. A., Msadek, R., Mueller, W. A., Taylor, K. E., Zwiers, F., Rixen, M., Ruprich-Robert, Y., and Eade, R.: The Decadal Climate Prediction Project (DCPP) contribution to CMIP6, Geoscientific Model Development, 9, 3751–3777, https://doi.org/10.5194/gmd-9-3751-2016, 2016.

Browne, P. A., De Rosnay, P., Zuo, H., Bennett, A., and Dawson, A.: Weakly coupled ocean–atmosphere data assimilation in the ECMWF NWP system, Remote Sensing, 11, 234, https://doi.org/10.3390/rs11030234, 2019.

Carton, J. A. and Giese, B. S.: A reanalysis of ocean climate using Simple Ocean Data Assimilation (SODA), Monthly Weather Review, 136, 2999–3017, https://doi.org/10.1175/2007MWR1978.1, 2008.

Chiang, J. C. H. and Sobel, A. H.: Tropical tropospheric temperature variations caused by ENSO and their influence on the remote tropical climate, Journal of Climate, 15, 2616–2631, https://doi.org/10.1175/1520-0442(2002)015<2616:TTTVCB>2.0.CO;2, 2002.

Chikamoto, Y., Timmermann, A., Widlansky, M. J., Zhang, S., and Balmaseda, M. A.: A drift-free decadal climate prediction system for the Community Earth System Model, Journal of Climate, 32, 5967–5995, https://doi.org/10.1175/JCLI-D-18-0788.1, 2019.

Craig, A. P., Vertenstein, M., and Jacob, R.: A new flexible coupler for Earth system modeling developed for CCSM4 and CESM1, The International Journal of High Performance Computing Applications, 26, 31–42, https://doi.org/10.1177/1094342011428141, 2012.

Doblas-Reyes, F. J., Andreu-Burillo, I., Chikamoto, Y., García-Serrano, J., Guemas, V., Kimoto, M., Mochizuki, T., Rodrigues, L. R. L., and van Oldenborgh, G. J.: Initialized near-term regional climate change prediction, Nature Communications, 4, 1715, https://doi.org/10.1038/ncomms2704, 2013.

Douville, H., Voldoire, A., and Geoffroy, O.: The recent global warming hiatus: What is the role of Pacific variability? Geophysical Research Letters, 42, 880–888, https://doi.org/10.1002/2014GL062775, 2015.

Eyring, V., Bony, S., Meehl, G. A., Senior, C. A., Stevens, B., Stouffer, R. J., and Taylor, K. E.: Overview of the Coupled Model Intercomparison Project Phase 6 (CMIP6) experimental design and organization, Geoscientific Model Development, 9, 1937–1958, https://doi.org/10.5194/gmd-9-1937-2016, 2016.

Feng, X., Haines, K., and de Boisséson, E.: Coupling of surface air and sea surface temperatures in the CERA-20C reanalysis, Quarterly Journal of the Royal Meteorological Society, 144, 195–207, https://doi.org/10.1002/qj.3194, 2018.

Golaz, J. C., Caldwell, P. M., Van Roekel, L. P., Petersen, M. R., Tang, Q., Wolfe, J. D., Abeshu, G., Anantharaj, V., Asay-Davis, X. S., Bader, D. C., Baldwin, S. A., Bisht, G., Bogenschutz, P. A., Branstetter, M., Brunke, M. A., Brus, S. R., Burrows, S. M., Cameron-Smith, P. J., Donahue, A. S., Deakin, M., Easter, R. C., Evans, K. J., Feng, Y., Flanner, M., Foucar, J. G., Fyke, J. G., Griffin, B. M., Hannay, C., Harrop, B. E., Hoffman, M. J., Hunke, E. C., Jacob, R. L., Jacobsen, D. W., Jeffery, N., Jones, P. W., Keen, N. D., Klein, S. A., Larson, V. E., Leung, L. R., Li, H. Y., Lin, W., Lipscomb, W. H., Ma, P. L., Mahajan, S., Maltrud, M. E., Mametjanov, A., McClean, J. L., McCoy, R. B., Neale, R. B., Price, S. F., Qian, Y., Rasch, P. J., Reeves Eyre, J. E. J., Riley, W. J., Ringler, T. D., Roberts, A. F., Roesler, E. L., Salinger, A. G., Shaheen, Z., Shi, X., Singh, B., Tang, J., Taylor, M. A., Thornton, P. E., Turner, A. K., Veneziani, M., Wan, H., Wang, H., Wang, S., Williams, D. N., Wolfram, P. J., Worley, P. H., Xie, S., Yang, Y., Yoon, J.-H., Zelinka, M. D., Zender, C. S., Zeng, X., Zhang, C., Zhang, K., Zhang, Y., Zheng, X., Zhou, T., and Zhu, Q.: The DOE E3SM Coupled Model Version 1: Overview and Evaluation at Standard Resolution, Journal of Advances in Modeling Earth Systems, 11, 2089–2129, https://doi.org/https://doi.org/10.1029/2018MS001603, 2019.

Golaz, J. C., Van Roekel, L. P., Zheng, X., Roberts, A. F., Wolfe, J. D., Lin, W. Y., Bradley, A. M., Tang, Q., Maltrud, M. E., Forsyth, R. M., Zhang, C. Z., Zhou, T., Zhang, K., Zender,

C. S., Wu, M. X., Wang, H. L., Turner, A. K., Singh, B., Richter, J. H., Qin, Y., Petersen, M. R., Mametjanov, A., Ma, P., Larson, V. E., Krishna, J., Keen, N. D., Jeffery, N., Hunke, E. C., Hannah, W. M., Guba, O., Griffin, B. M., Feng, Y., Engwirda, D., Vittorio, A. V., Cheng, D., Conlon, L. M., Chen, C., Brunke, M. A., Bisht, G., Benedict, J. J., Asay-Davis, X. S., Zhang, Y. Y., Zhang, M., Zeng, X. B., Xie, S. C., Wolfram, P. J., Vo, T., Veneziani, M., Tesfa, T. K., Sreepathi, S., Salinger, A. G., Jack Reeves Eyre, J. E., Prather, M. J., Mahajan, S., Li, Q., Jones, P. W., Jacob, R. L., Huebler, G. W., Huang, X. L., Hillman, B. R., Harrop, B. E., Foucar, J. G., Fang, Y. L., Comeau, D. S., Caldwell, P. M., Bartoletti, T., Balaguru, K., Taylor, M. A., McCoy, R. B., Leung, L. R., and Bader, D. C.: The DOE E3SM Model version 2: Overview of the physical model and initial model evaluation, Journal of Advances in Modeling Earth Systems, 14, e2022MS003156, https://doi.org/10.1029/2022MS003156, 2022.

Good, S. A., Martin, M. J., and Rayner, N. A.: EN4: Quality controlled ocean temperature and salinity profiles and monthly objective analyses with uncertainty estimates, Journal of Geophysical Research: Oceans, 118(12), 6704–6716, https://doi.org/10.1002/2013JC009067, 2013.

Han, G., Wu, X., Zhang, S., Liu, Z., and Li, W.: Error covariance estimation for coupled data assimilation using a Lorenz atmosphere and a simple pycnocline ocean model, Journal of Climate, 26, 10218–10231, https://doi.org/10.1175/JCLI-D-13-00236.1, 2013.

Hanley, D. E., Bourassa, M. A., O'Brien, J. J., Smith, S. R., and Spade, E. R.: A quantitative evaluation of ENSO indices, Journal of Climate, 16, 1249–1258, https://doi.org/10.1175/1520-0442(2003)16<1249:AQEOEI>2.0.CO;2, 2003.

Hersbach, H., Bell, B., Berrisford, P., Hirahara, S., Horányi, A., Muñoz-Sabater, J., Nicolas, J., Peubey, C., Radu, R., Schepers, D., Simmons, A., Soci, C., Abdalla, S., Abellan, X., Balsamo, G., Bechtold, P., Biavati, G., Bidlot, J., Bonavita, M., De Chiara, G., Dahlgren, P., Dee, D., Diamantakis, M., Dragani, R., Flemming, J., Forbes, R., Fuentes, M., Geer, A., Haimberger, L., Healy, S., Hogan, R. J., Hólm, E., Janisková, M., Keeley, S., Laloyaux, P., Lopez, P., Lupu, C., Radnoti, G., de Rosnay, P., Rozum, I., Vamborg, F., Villaume, S., and Thépaut, J.-N.: The ERA5 global reanalysis, Quarterly Journal of the Royal

Meteorological Society, 146, 1999–2049, https://doi.org/10.1002/qj.3803, 2020.

He, Y., Wang, B., Liu, M., Liu, L., Yu, Y., Liu, J., Li, R., Zhang, C., Xu, S., Huang, W., Liu, Q., Wang, Y., and Li, F.: Reduction of initial shock in decadal predictions using a new initialization strategy, Geophysical Research Letters, 44(16), 8538–8547, https://doi.org/10.1002/2017GL074028, 2017.

He, Y., Wang, B., Huang, W., Xu, S., Wang, Y., Liu, L., Li, L., Liu, J., Yu, Y., Lin, Y., Huang, X., and Peng, Y.: A new DRP-4DVar-based coupled data assimilation system for decadal predictions using a fast online localization technique, Climate Dynamics, 54, 3541–3559, https://doi.org/10.1007/s00382-020-05190-w, 2020.

Higgins, R. W., Leetmaa, A., Xue, Y., and Barnston, A.: Dominant factors influencing the seasonal predictability of U.S. precipitation and surface air temperature, Journal of Climate, 13, 3994–4017, https://doi.org/10.1175/1520-0442(2000)013<3994:DFITSP>2.0.CO;2, 2000.

Ju, X., Chen, S., Chen, W., Wu, R., Chen, L., and Cheng, X.: Origins of the overestimated Indian Ocean Dipole amplitude in current coupled climate models, Climate Dynamics, 63, 180, https://doi.org/10.1007/s00382-025-07673-0, 2025.

Kim, Y.-Y., Lee, J.-Y., Chikamoto, Y., Timmermann, A., Lee, S.-S., Kwon, E. Y., Park, W., Hasan, N. A., Bethke, I., Fransner, F., Karwat, A., Subrahmanian, A. R., and Franzke, C. L. E.: Robust estimates of Earth system predictability of the first kind using the CESM2 multiyear prediction system (CESM2-MP), Bulletin of the American Meteorological Society, 106, 2087–2109, https://doi.org/10.1175/BAMS-D-24-0329.1, 2025.

Kosaka, Y. and Xie, S. P.: The tropical Pacific as a key pacemaker of the variable rates of global warming, Nature Geoscience, 9(9), 669–673, https://doi.org/10.1038/ngeo2770, 2016.

Leung, L. R., Bader, D. C., Taylor, M. A., and McCoy, R. B.: An introduction to the E3SM special collection: Goals, science drivers, development, and analysis, Journal of Advances in Modeling Earth Systems, 12, e2019MS001821, https://doi.org/10.1029/2019MS001821, 2020.

Li, H., Wigmosta, M. S., Wu, H., Huang, M., Ke, Y., Coleman, A. M., and Leung, L. R.: A physically based runoff routing model for land surface and Earth system models, Journal of Hydrometeorology, 14, 808–828, https://doi.org/10.1175/JHM-D-12-015.1, 2013.

Lin, L. F. and Pu, Z.: Examining the impact of SMAP soil moisture retrievals on short-range weather prediction under weakly and strongly coupled data assimilation with WRF-Noah, Monthly Weather Review, 147, 4345–4366, https://doi.org/10.1175/MWR-D-19-0017.1, 2019.

Lin, L. F. and Pu, Z.: Improving near-surface short-range weather forecasts using strongly coupled land–atmosphere data assimilation with GSI-EnKF, Monthly Weather Review, 148, 2863-2888, https://doi.org/10.1175/MWR-D-19-0370.1, 2020.

Liu, J., Wang, B., and Xiao, Q.: An evaluation study of the DRP-4DVar approach with the Lorenz-96 model, Tellus A: Dynamic Meteorology and Oceanography, 63, 256–262, https://doi.org/10.1111/j.1600-0870.2010.00487.x, 2011.

Mantua, N. J., Hare, S. R., Zhang, Y., Wallace, J. M., and Francis, R. C.: A Pacific interdecadal climate oscillation with impacts on salmon production, Bulletin of the American Meteorological Society, 78, 1069–1080, https://doi.org/10.1175/1520-0477(1997)078<1069:APICOW>2.0.CO;2, 1997.

Meehl, G. A., Richter, J. H., Teng, H., Capotondi, A., Cobb, K., Doblas-Reyes, F., Donat, M. G., England, M. H., Fyfe, J. C., Han, W., Kim, H., Kirtman, B. P., Kushnir, Y., Lovenduski, N. S., Mann, M. E., Merryfield, W. J., Nieves, V., Pegion, K., Rosenbloom, N., Sanchez, S. C., Scaife, A. A., Smith, D., Subramanian, A. C., Sun, L., Thompson, D., Ummenhofer, C. C., and Xie, S.-P.: Initialized Earth system prediction from subseasonal to decadal timescales, Nature Reviews Earth & Environment, 2, 340–357, https://doi.org/10.1038/s43017-021-00155-x, 2021.

Morioka, Y., Doi, T., Storto, A., Masina, S., and Behera, S. K.: Role of subsurface ocean in decadal climate predictability over the South Atlantic, Scientific Reports, 8, 8523, https://doi.org/10.1038/s41598-018-26899-z, 2018.

Mulholland, D. P., Laloyaux, P., Haines, K., and Balmaseda, M. A.: Origin and impact of initialization shocks in coupled atmosphere–ocean forecasts, Monthly Weather Review, 143, 4631–4644, https://doi.org/10.1175/MWR-D-15-0076.1, 2015.

Penny, S. G., Bach, E., Bhargava, K., Chang, C.-C., Da, C., Sun, L., and Yoshida, T.: Strongly coupled data assimilation in multiscale media: Experiments using a quasi-geostrophic coupled model, Journal of Advances in Modeling Earth Systems, 11, 1803–1829, https://doi.org/10.1029/2019MS001652, 2019.

Rayner, N. A., Parker, D. E., Horton, E. B., Folland, C. K., Alexander, L. V., Rowell, D. P., Kent, E. C., and Kaplan, A.: Global analyses of sea surface temperature, sea ice, and night marine air temperature since the late nineteenth century, Journal of Geophysical Research: Atmospheres, 108, 4407, https://doi.org/10.1029/2002JD002670, 2003.

Reckinger, S. M., Petersen, M. R., and Reckinger, S. J.: A study of overflow simulations using MPAS-Ocean: Vertical grids, resolution, and viscosity, Ocean Modelling, 96, 291–313, https://doi.org/10.1016/j.ocemod.2015.09.006, 2015.

Ropelewski, C. F. and Halpert, M. S.: North American precipitation and temperature patterns associated with the El Niño/Southern Oscillation (ENSO), Monthly Weather Review, 114, 2352–2362, https://doi.org/10.1175/1520-0493(1986)114<2352:NAPATP>2.0.CO;2, 1986.

Saji, N. H., Goswami, B. N., Vinayachandran, P. N., and Yamagata, T.: A dipole mode in the tropical Indian Ocean, Nature, 401, 360–363, https://doi.org/10.1038/43854, 1999.

Saji, N. H., Xie, S.-P., and Yamagata, T.: Tropical Indian Ocean variability in the IPCC twentieth-century climate simulations, Journal of Climate, 19, 4397–4417, https://doi.org/10.1175/JCLI3847.1, 2006.

Shi, P., Lu, H., Leung, L.R., He, Y., Wang, B., Yang, K., Yu, L., Liu, L., Huang, W., Xu, S., Liu, J., Huang, X., Li, L., and Lin, Y.: Significant land contributions to interannual predictability of East Asian summer monsoon rainfall, Earth's Future, 9(2), e2020EF001762, https://doi.org/10.1029/2020EF001762, 2021.

Shi, P., Wang, B., He, Y., Lu, H., Yang, K., Xu, S. M., Huang, W. Y., Liu, L., Liu, J. J., Li, L. J., and Wang, Y.: Contributions of weakly coupled data assimilation–based land initialization to interannual predictability of summer climate over Europe, Journal of Climate, 35, 517–535, https://doi.org/10.1175/JCLI-D-20-0506.1, 2022.

Shi, P., Leung, L. R., Wang, B., Zhang, K., Hagos, S. M., and Zhang, S.: The 4DEnVar-based weakly coupled land data assimilation system for E3SM version 2, Geoscientific Model

Development, 17, 3025–3040, https://doi.org/10.5194/gmd-17-3025-2024, 2024a.

Shi, P., Leung, L. R., Lu, H., Wang, B., Yang, K., and Chen, H.: Uncovering the interannual predictability of the 2003 European summer heatwave linked to the Tibetan Plateau, npj Climate and Atmospheric Science, 7, 242, https://doi.org/10.1038/s41612-024-00782-3, 2024b.

Shi, P., Leung, L. R., and Wang, B.: Development and evaluation of a new 4DEnVar-based weakly coupled ocean data assimilation system in E3SMv2, Geoscientific Model Development, 18, 2443–2460, https://doi.org/10.5194/gmd-18-2443-2025, 2025.

Sluka, T. C., Penny, S. G., Kalnay, E., and Miyoshi, T.: Assimilating atmospheric observations into the ocean using strongly coupled ensemble data assimilation, Geophysical Research Letters, 43, 752–759, https://doi.org/10.1002/2015GL067238, 2016.

Tang, Q., Mu, L., Goessling, H. F., Semmler, T., and Nerger, L.: Strongly coupled data assimilation of ocean observations into an ocean-atmosphere model, Geophysical Research Letters, 48, e2021GL094941, https://doi.org/10.1029/2021GL094941, 2021.

Taylor, K. E., Stouffer, R. J., and Meehl, G. A.: An overview of CMIP5 and the experiment design, Bulletin of the American Meteorological Society, 93, 485–498, https://doi.org/10.1175/BAMS-D-11-00094.1, 2012.

Trenberth, K. E. and Stepaniak, D. P.: Indices of El Niño evolution, Journal of Climate, 14, 1697–1701, https://doi.org/10.1175/1520-0442(2001)014<1697:LIOENO>2.0.CO;2, 2001.

Trenberth, K. E. and Shea, D. J.: Atlantic hurricanes and natural variability in 2005, Geophysical Research Letters, 33, L12704, https://doi.org/10.1029/2006GL026894, 2006.

Turner, A. K., Lipscomb, W. H., Hunke, E. C., Jacobsen, D. W., Jeffery, N., Engwirda, D., Ringler, T. D., and Wolfe, J. D.: MPAS-Seaice (v1.0.0): Sea-ice dynamics on unstructured Voronoi meshes, Geoscientific Model Development, 15, 3721–3751, https://doi.org/10.5194/gmd-15-3721-2022, 2022.

Wang, B., Liu, J., Wang, S., Cheng, W., Liu, J., Liu, C., Xiao, Q., and Kuo, Y. H.: An economical approach to four-dimensional variational data assimilation, Advances in Atmospheric Sciences, 27, 715–727, https://doi.org/10.1007/s00376-009-9122-3, 2010.

Wang, C.: Three-ocean interactions and climate variability: A review and perspective, Climate Dynamics, 53, 5119–5136, https://doi.org/10.1007/s00382-019-04930-x, 2019.

Wu, B., Zhou, T., and Zheng, F.: EnOI-IAU initialization scheme designed for decadal climate prediction system IAP-DecPreS, Journal of Advances in Modeling Earth Systems, 10, 342–356, https://doi.org/10.1002/2017MS001132, 2018.

Zhang, S.: A study of impacts of coupled model initial shocks and state–parameter optimization on climate predictions using a simple pycnocline prediction model, Journal of Climate, 24, 6210–6226, https://doi.org/10.1175/JCLI-D-10-05003.1, 2011.

Zhang, S., Liu, Z., Rosati, A., and Delworth, T.: A study of enhancive parameter correction with coupled data assimilation for climate estimation and prediction using a simple coupled model, Tellus A: Dynamic Meteorology and Oceanography, 64, 10963, https://doi.org/10.3402/tellusa.v64i0.10963, 2012.

Zhang, S., Liu, Z., Zhang, X., Wu, X., Han, G., Zhao, Y., Yu, X., Liu, C., Liu, Y., Wu, S., Lu, F., Li, M., and Deng, X.: Coupled data assimilation and parameter estimation in coupled ocean–atmosphere models: A review, Climate Dynamics, 54, 5127–5144, https://doi.org/10.1007/s00382-020-05275-6, 2020.

Zhou, W., Li, J., Yan, Z., Shen, Z., Wu, B., Wang, B., Zhang, R., and Li, Z.: Progress and future prospects of decadal prediction and data assimilation: A review, Atmospheric and Oceanic Science Letters, 17, 100441, https://doi.org/10.1016/j.aosl.2023.100441, 2024.

Zhu, J., Kumar, A., Lee, H.-C., and Wang, H.: Seasonal predictions using a simple ocean initialization scheme, Climate Dynamics, 49, 3989–4007, https://doi.org/10.1007/s00382-017-3556-6, 2017.

Zhu, S., Wang, B., Zhang, L., Liu, J., Liu, Y., Gong, J., Xu, S., Wang, Y., Huang, W., Liu, L., He, Y., and Wu, X.: A Four-Dimensional Ensemble-Variational (4DEnVar) Data Assimilation System Based on GRAPES-GFS: System Description and Primary Tests, Journal of Advances in Modeling Earth Systems, 14(7), e2021MS002737, https://doi.org/10.1029/2021MS002737, 2022.

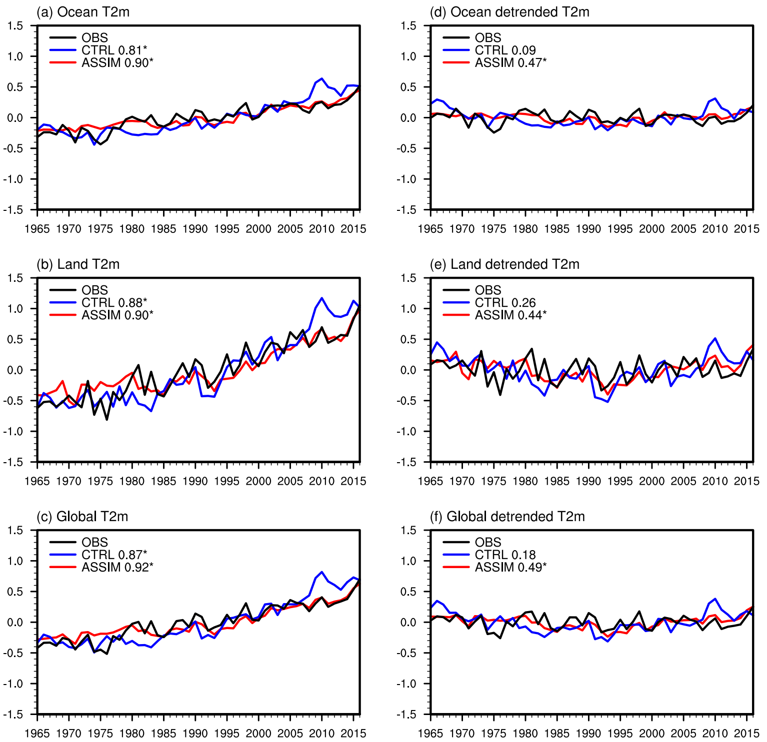


**Figure 1.** Time series of non-detrended (left column) and linearly detrended (right column) annual mean surface air temperature anomalies (units: °C) over (a, d) ocean, (b, e) land, and (c, f) global domains from 1965 to 2016. Black line: observation; blue line: CTRL; red line: ASSIM. Temperature anomalies are computed by removing the climatological mean. For the detrended series, a linear trend is removed from the domain-averaged time series. The correlation coefficients of CTRL and ASSIM with the observation are also shown. The asterisk denotes statistically significant correlation at the 95% confidence level.

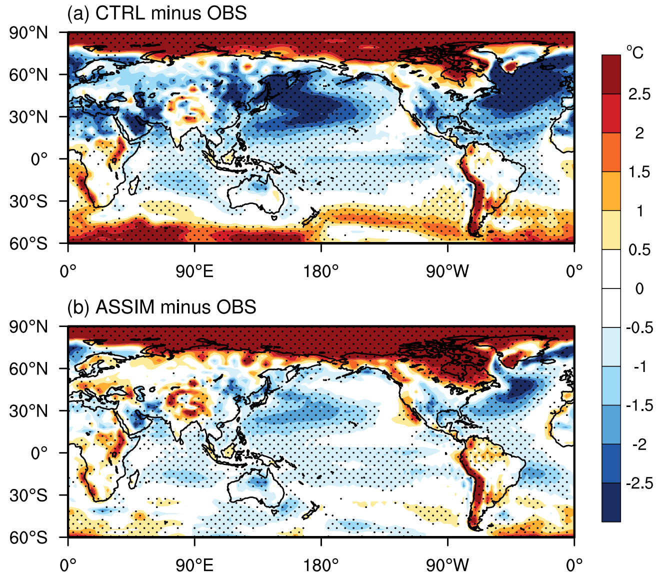


**Figure 2.** Spatial patterns of climatological mean differences in surface air temperature (units: °C) between model simulations and observations for the period 1965–2016. Panel (a) shows the difference between CTRL and observation, and panel (b) shows the difference between ASSIM and observation. Dotted areas denote regions where the differences are statistically significant at the 95% confidence level.

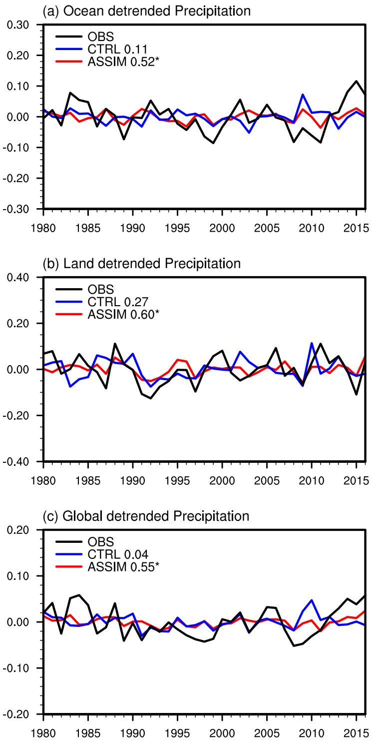


**Figure 3.** Time series of linearly detrended annual mean precipitation anomalies (units: mm day$^{-1}$) over (a) ocean, (b) land, and (c) global domains from 1980 to 2016. Black line: observation; blue line: CTRL; red line: ASSIM. Precipitation anomalies are computed by removing both the climatological mean and long-term trend. For the detrended series, a linear trend is removed from the domain-averaged time series. The correlation coefficients of CTRL and ASSIM with the observation are also shown. The asterisk denotes statistically significant correlation at the 95% confidence level.

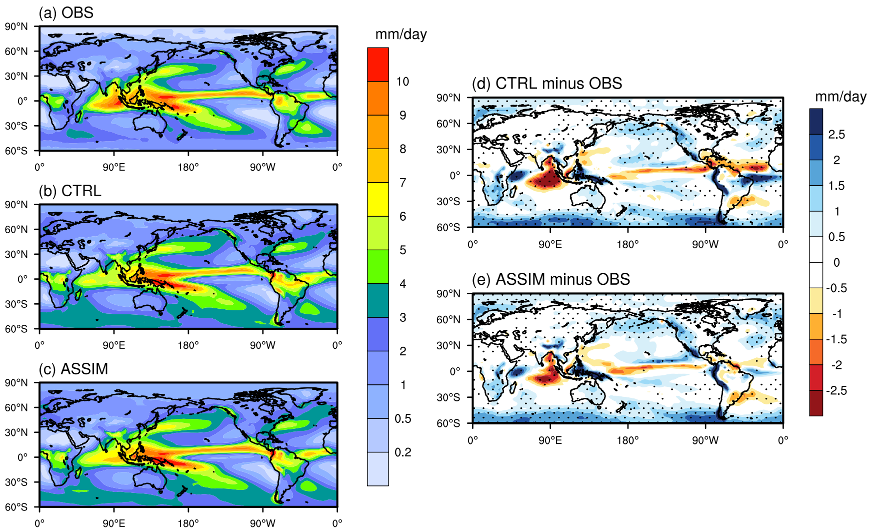


**Figure 4.** Spatial patterns of (a–c) climatological mean precipitation (units: mm day$^{-1}$) and (d, e) precipitation differences for the period 1980–2016. Panels (a–c) show precipitation climatology from observation, CTRL, and ASSIM, respectively. Panels (d, e) represent precipitation differences between model simulations and observations: (d) CTRL minus observation and (e) ASSIM minus observation. Dotted areas indicate regions where the differences are statistically significant at the 95% confidence level.

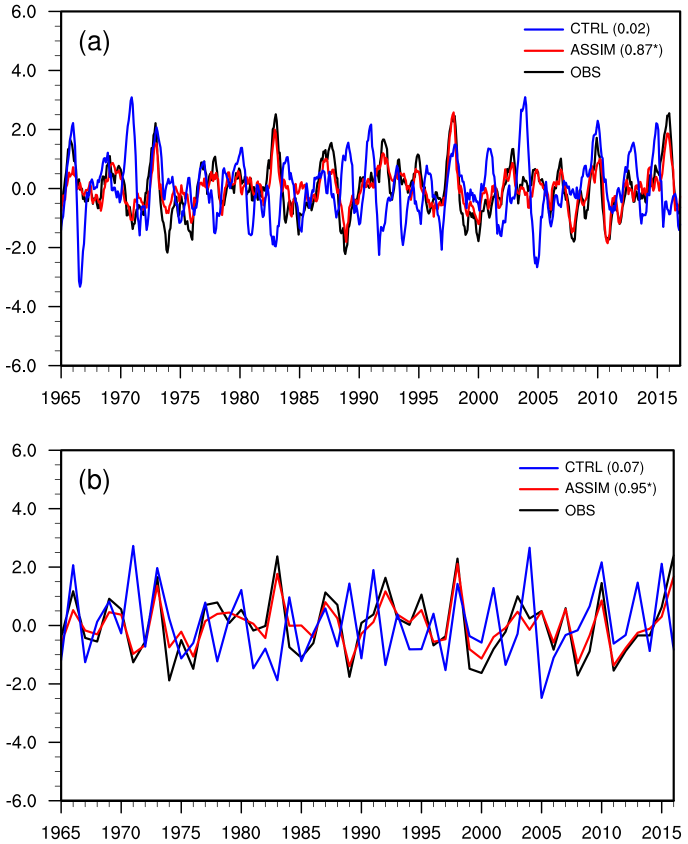


**Figure 5.** Time series of the (a) monthly and (b) winter Niño 3.4 index from 1965 to 2016 for the observation (black line), ASSIM (red line), and CTRL (blue line). The correlation coefficients with the observation for ASSIM and CTRL are also shown in parentheses. The asterisk indicates that the correlation is statistically significant at the 95% confidence level.

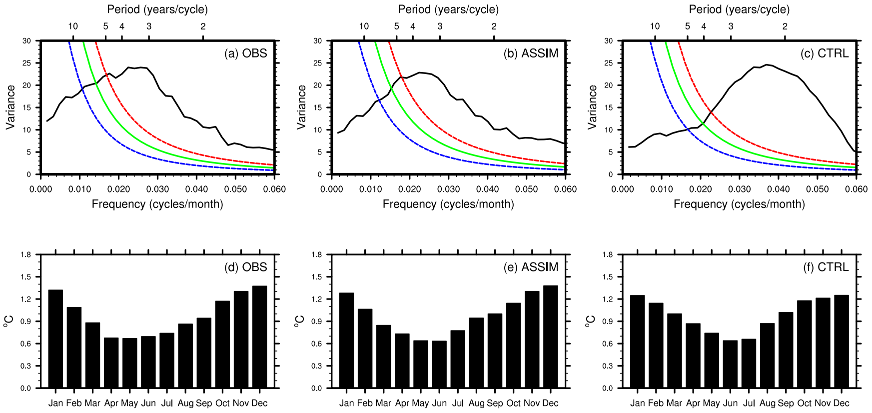


**Figure 6.** Power spectra (a–c) and seasonal cycle of the standard deviation (d–f) of the monthly Niño 3.4 index from the observation (left column), ASSIM (middle column), and CTRL (right column) for the period 1965–2016. The theoretical Markov "red noise" spectrum is shown as a solid green line, with the 5% and 95% confidence bounds indicated by dashed blue and red lines, respectively.

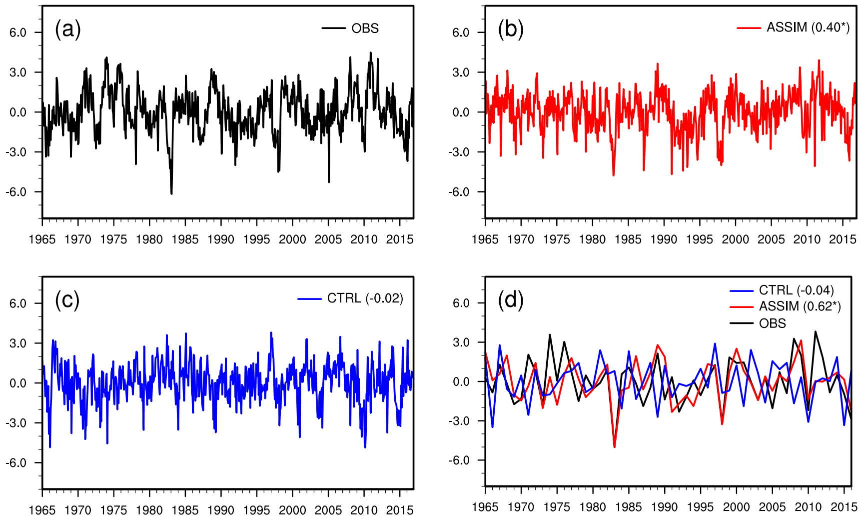


**Figure 7.** Time series of the (a–c) monthly and (d) winter Southern Oscillation Index (SOI) from 1965 to 2016 for the observation (black line), ASSIM (red line), and CTRL (blue line). Panels (a–c) show individual monthly time series from observation, ASSIM, and CTRL, respectively, while panel (d) shows the winter SOI averaged over December–February (DJF). The correlation coefficients with the observation in ASSIM and CTRL are also indicated in parentheses. The asterisk indicates that the correlation is statistically significant at the 95% confidence level.

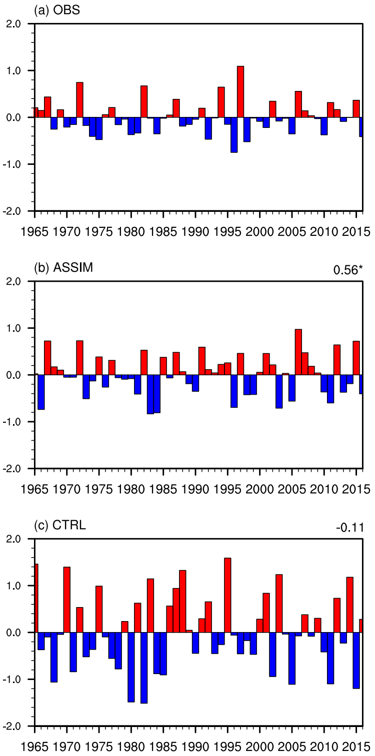


**Figure 8.** Time series of the autumn (September–November) Dipole Mode Index (DMI) from 1965 to 2016 for (a) the observation, (b) ASSIM, and (c) CTRL. The correlation coefficients of ASSIM and CTRL with the observed DMI are also shown in the upper-right corner. The asterisk indicates that the correlation is statistically significant at the 95% confidence level.

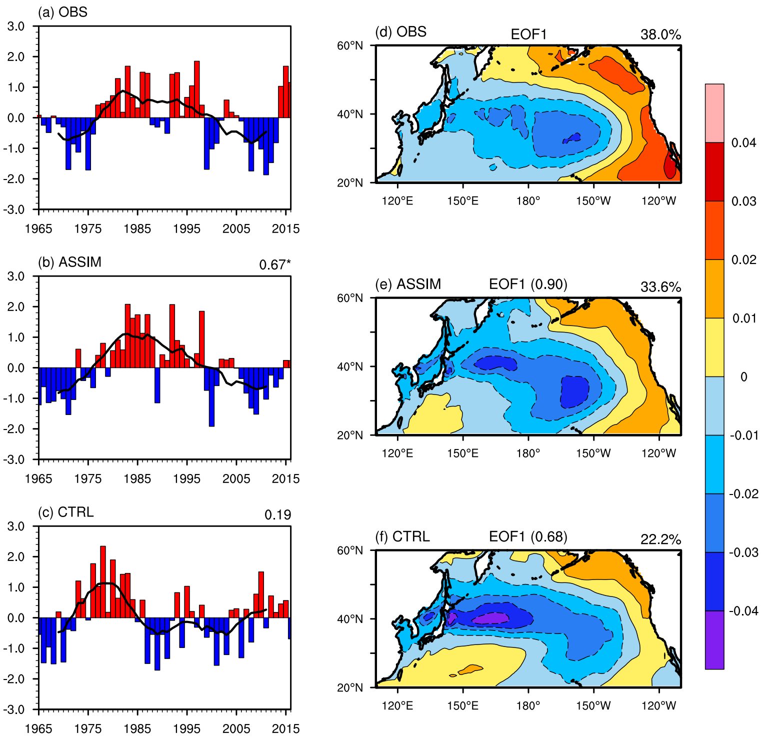


**Figure 9.** Time series and spatial patterns of the Pacific Decadal Oscillation (PDO) index from 1965 to 2016 for (a, d) the observation, (b, e) ASSIM, and (c, f) CTRL. The black lines in panels (a–c) denote the 10-year running mean of the annual PDO index. The numbers at the top right of (b) and (c) indicate the temporal correlations of ASSIM and CTRL with observations. The asterisk indicates that the temporal correlation is statistically significant at the 95% confidence level. The percentage of variance explained by EOF1 is shown at the top right of (d–f), and the numbers at the top center of (e) and (f) indicate the spatial correlations with the observed pattern. The EOF analysis is performed separately for the observations and model outputs after interpolating both onto a common horizontal grid and removing linear trends at each grid point.

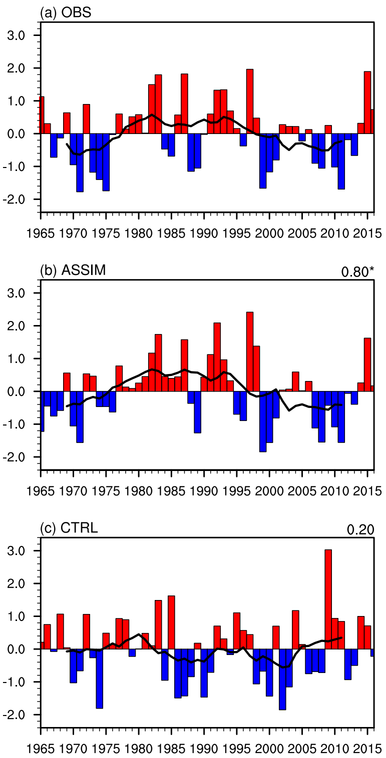


**Figure 10.** Time series of the Interdecadal Pacific Oscillation (IPO) index from 1965 to 2016 for (a) the observation, (b) ASSIM, and (c) CTRL. The black line in each panel denotes the 10-year running mean of the annual IPO index. The numbers at the top right of (b) and (c) indicate the temporal correlations of ASSIM and CTRL with observations. The asterisk indicates that the temporal correlation is statistically significant at the 95% confidence level. The IPO index is derived from EOF analysis after interpolating both the observations and model outputs onto a common horizontal grid and removing linear trends at each grid point.

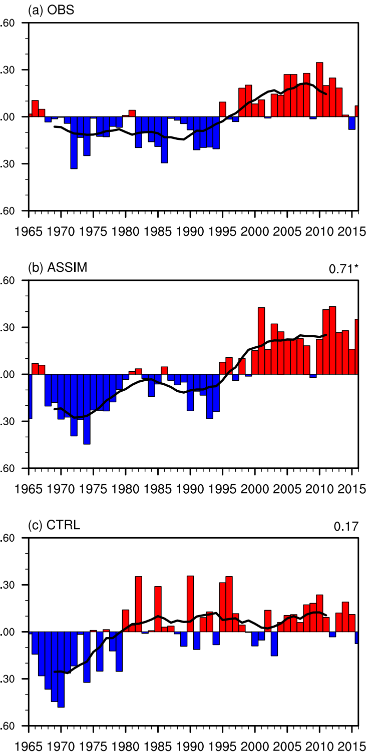


**Figure 11.** Time series of the Atlantic Multidecadal Oscillation (AMO) index from 1965 to 2016 for (a) the observation, (b) ASSIM, and (c) CTRL. The black line denotes the 10-year running mean. The numbers at the top right of (b) and (c) indicate the temporal correlations of ASSIM and CTRL with observations. The asterisk indicates that the correlation is statistically significant at the 95% confidence level. The AMO index is calculated by subtracting the global mean SST anomalies (60°S–60°N) from the North Atlantic SST anomalies (0–60°N, 0–80°W).

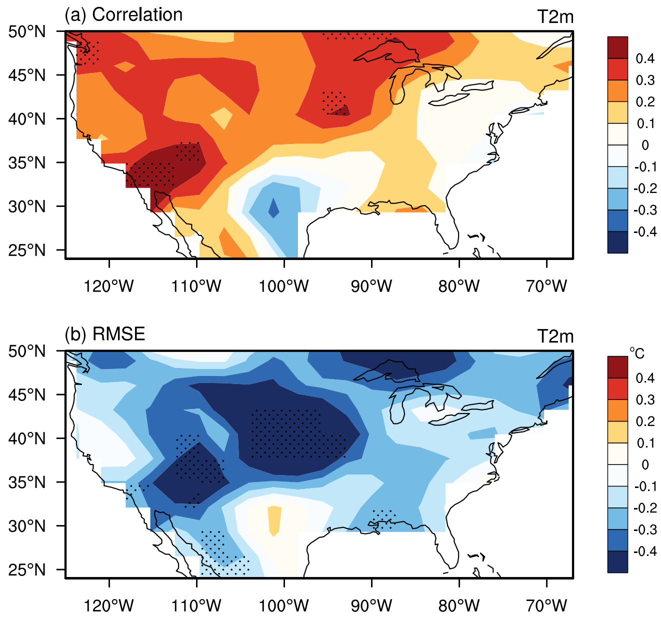


**Figure 12.** Spatial patterns of the differences in (a) correlation coefficients and (b) root-mean-square errors (RMSE; °C) of detrended winter surface air temperature anomalies between ASSIM and CTRL with observations from 1980 to 2016 over the contiguous U.S. Dotted areas indicate regions where the differences are statistically significant at the 95% confidence level.

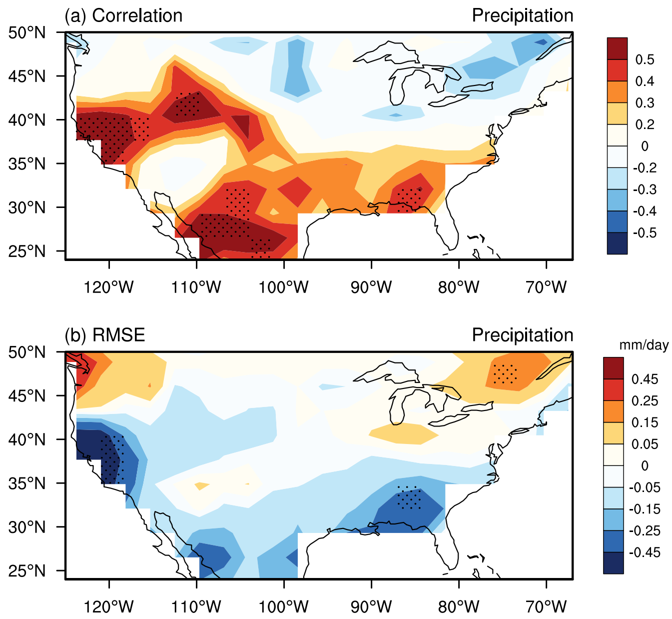


**Figure 13.** Similar to Fig. 12 but for detrended winter precipitation. Dotted areas denote regions where the differences pass the 95% confidence level.

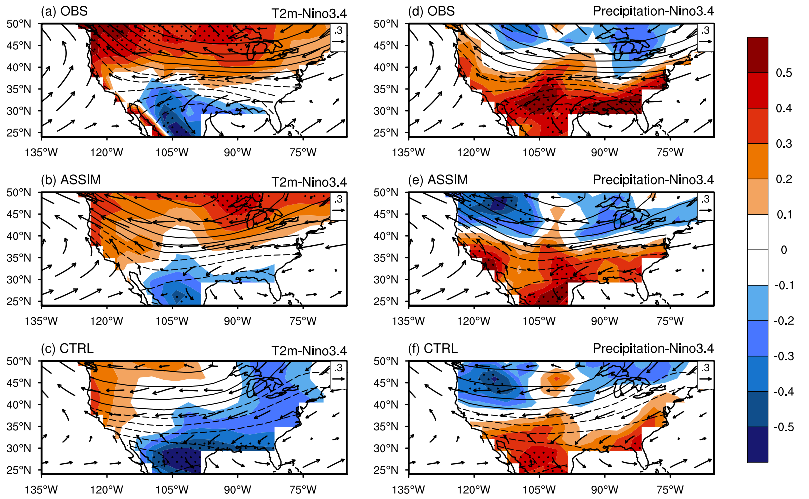


**Figure 14.** Regression patterns of winter surface air temperature (left column; shaded) and precipitation (right column; shaded), 500hPa geopotential height (contours), and 850hPa winds (vectors) on the standardized winter Niño 3.4 index from 1980 to 2016 for (a, d) the observation, (b, e) ASSIM, and (c, f) CTRL. In each panel, the Niño 3.4 index is calculated separately from its corresponding dataset and all regressions are based on simultaneous winter (DJF) averages. Dotted areas indicate regions where the regressions are statistically significant at the 95% confidence level.

**Appendix A: Supporting Information**

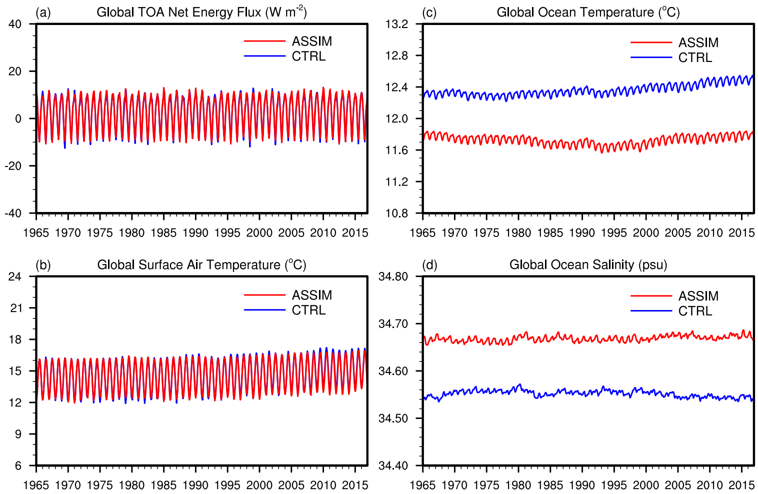


**Figure A1.** Time series of (a) global mean top-of-atmosphere (TOA) net energy flux (W $m^{-2}$), (b) global mean surface air temperature (°C), (c) global mean ocean temperature averaged over the upper 1000 m (°C), and (d) global mean ocean salinity averaged over the upper 1000 m (psu). The blue and red lines denote the CTRL and ASSIM, respectively.

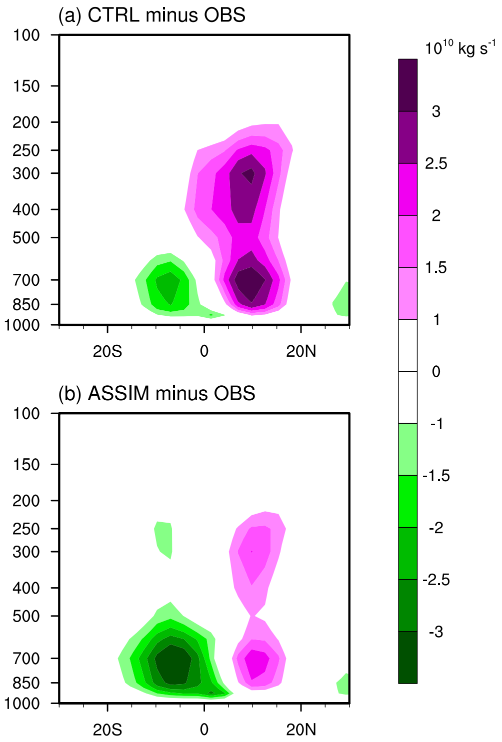


**Figure A2.** Zonal-mean meridional streamfunction differences (units: $10^{10}$ kg s$^{-1}$) between model simulations and observations averaged over the period 1980–2016. Panel (a) shows the difference between CTRL and observations, and panel (b) shows the difference between ASSIM and observations. The vertical axis represents pressure levels (hPa), and the horizontal axis denotes latitude.

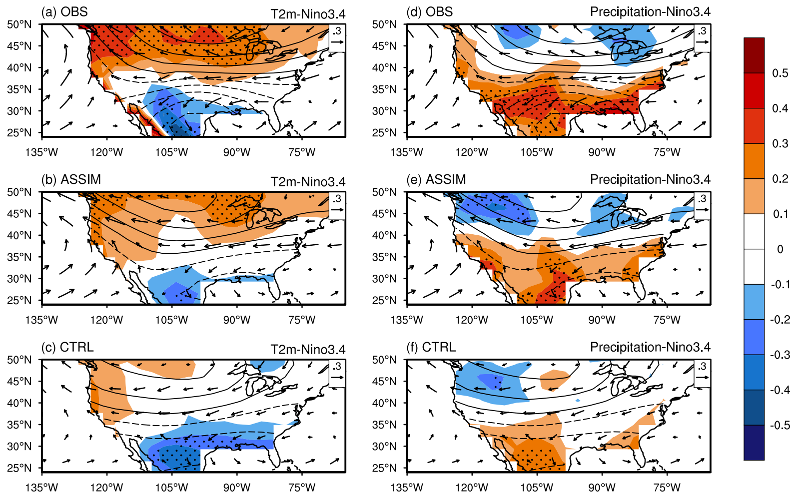


**Figure A3.** Lagged regression patterns of monthly winter (DJF) surface air temperature (left column; shaded), precipitation (right column; shaded), 500hPa geopotential height (contours), and 850hPa winds (vectors) onto the preceding month's (NDJ) standardized Niño 3.4 index for (a, d) the observation, (b, e) ASSIM, and (c, f) CTRL. Specifically, monthly atmospheric variables from December to February (DJF) are regressed onto the standardized monthly Niño 3.4 index from November to January (NDJ), corresponding to a one-month lead time. The Niño 3.4 index is calculated separately from each corresponding dataset. Dotted areas denote statistical significance at the 95% confidence level.

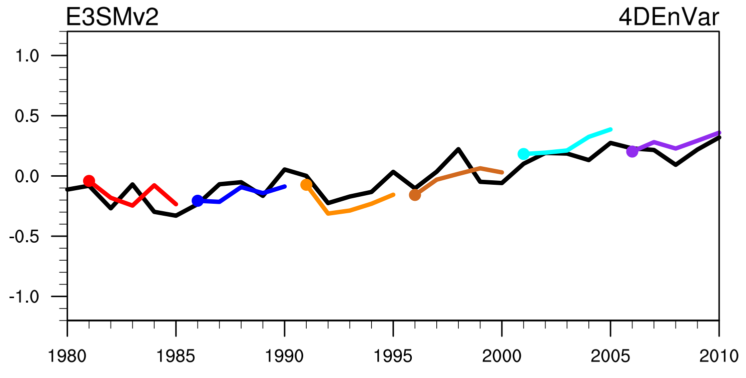


**Figure A4.** Time series of annual mean global average surface air temperature anomalies (units: °C) from 1980 to 2010. The black line denotes the observation, while the colored lines denote the ensemble mean hindcast experiments produced by E3SMv2 initialized with the 4DEnVar-based weakly coupled ocean data assimilation system. Each hindcast is initialized at the start of a different year (1981, 1986, 1991, 1996, 2001, and 2006; marked by filled circles) and is then integrated freely for five years. For each target initialization year, three ensemble members are initialized in the preceding September and November and in January of the target year. The ensemble mean is then computed from these three members throughout the entire five-year hindcast period.

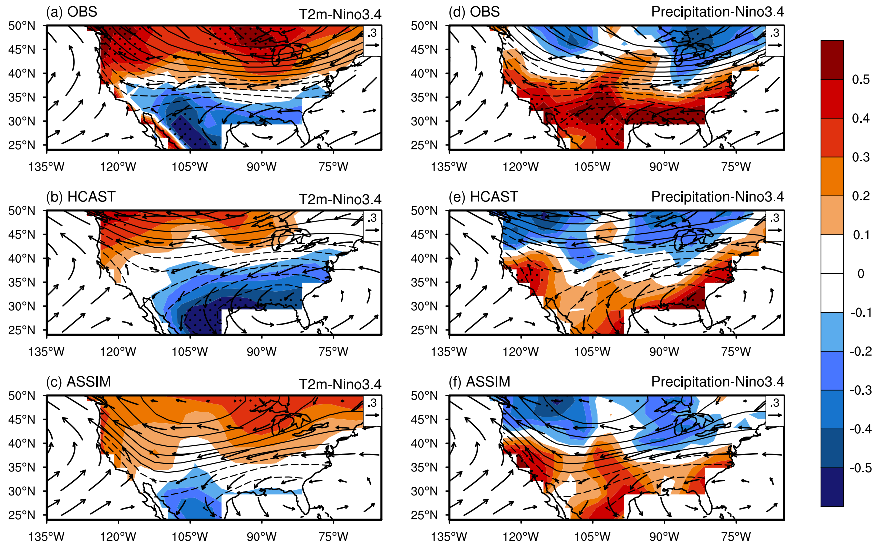


**Figure A5.** Regression patterns of winter surface air temperature (left column; shaded) and precipitation (right column; shaded), 500hPa geopotential height (contours), and 850hPa winds (vectors) on the standardized winter Niño 3.4 index from 1981 to 2010 for (a, d) the observation, (b, e) HCAST, and (c, f) ASSIM. The HCAST results are based on the ensemble mean hindcasts initialized at five-year intervals from 1981 to 2006, as described in Fig. A4. The successive five-year segments are then concatenated to form a continuous time series from 1981 to 2010, without any bias correction applied. Dotted areas indicate regions where the regressions are statistically significant at the 95% confidence level.